JOURNAL OF GEOPHYSICAL RESEARCH, VOL. 91, NO. B9, PAGES 9081–9098, AUGUST 10, 1986

Ocean Signals in Tide Gauge Records

DUDLEY B. CHELTON AND DAVID B. ENFIELD

College of Oceanography, Oregon State University, Corvallis

Tide gauges are designed to measure changes in water level relative to land. However, vertical motions of the earth's crust manifest themselves as apparent water level changes in tide gauge records. These crustally induced changes are often small in amplitude relative to the wide range of oceanic processes which affect water level in coastal regions. Vertical crustal motion can best be studied by first removing oceanic variability from the time series. In this paper we summarize the major oceanic signals in tide gauge records. We take the approach that the oceanic signals are unwanted "noise" in the data. Methods are described for removing or at least reducing the various oceanic signals. These oceanic signals span a broad range of time scales from tides to interannual variability associated with the El Niño phenomenon and secular sea level change from a number of oceanographic effects.

1. INTRODUCTION

Tide gauges have been used for over 100 years to measure the sea level height (SLH) relative to fixed bench marks. The tide gauges are referenced to bench marks located (whenever possible) in stable bedrock. This referencing is accomplished by precise first-order leveling through a succession of visual sightings, none of which exceed 150 m. Although explicitly named, it is sometimes easy to forget that tide gauges were originally designed for the study and prediction of tides. Nonetheless, these devices have proven useful for a much broader range of geophysical applications. Tide gauge data would be useful only for oceanographic applications if the bench mark remained fixed in space and time. However, since the water level measured by tide gauges is subject to rising and falling of the land as well as the sea, the tide gauge data can also be used to study vertical motion of the earth's crust. It is not always a simple task to distinguish apparent water level changes due to movement of a tide gauge from true water level changes due to oceanographic processes.

In this paper we review the full range of ocean signals in tide gauge records. In recognition of the fact that the readers of this paper will primarily be geophysicists interested in crustal motion, we take the approach that ocean signals are an unwanted "noise" in tide gauge records. Our objective is to describe the oceanographic signals which have been studied from tide gauge data and then to discuss methods for removing the ocean signals to draw out the "signal" of vertical crustal motion (which, of course, constitutes noise in oceanographic applications). Many of the ocean signals can easily be removed. Other ocean variability looks disturbingly similar to apparent water level changes due to crustal motion. It is crucial that analysts be aware of these limitations when using tide gauge data to infer crustal motion. The difficulty in distinguishing ocean signals from crustal signals has previously been discussed by *Vanicek* [1978].

Although tide gauges vary in design, they all utilize some filtering technique to remove short-period fluctuations in water level produced by surface gravity waves. Thus tide gauges provide information on water level variations at time scales of a few minutes and longer. In the most common design this low-pass-filtering operation is achieved by measuring the water level in a cylinder with a narrow opening at the bottom. This narow opening limits the rate at which the water level can change inside the cylinder. A potential problem with this design is that the orifice can become plugged with mud and silt or covered by living organisms. This results in spurious recorded values of water level. Routine maintenance is necessary to keep the orifice clean and the tide gauge record uncontaminated. Other problems with tide gauges include mechanical failure of the float device, jamming of the paper tape recorder, digitization error, sinking of piers on which tide gauges are generally located, and intentional changes in the location of the tide gauge or bench mark. The overall data quality varies greatly with station. Unfortunately, problems with tide gauges occasionally go unnoticed for considerable periods of time. Consequently, it is not uncommon to find gaps in tide gauge records which sometimes make analysis of the data difficult.

In the following sections we separately discuss all of the major oceanographic signals in tide gauge records. For each, we give a brief overview of the physical causes of the SLH signal. A thorough review of the theory behind each physical mechanism is beyond the scope of this paper. The discussion is limited either to qualitative remarks about the physics or to a discussion of the theory for simplified special cases. These simplified models are often very useful for elucidating the physical aspects of the signal. For each signal we discuss the typical amplitudes in tide gauge records and give references where more detailed discussions can be found. We also discuss methods of removing or at least reducing each ocean signal in order to focus attention on signals associated with vertical crustal motion.

2. TIDES

The simplest of all ocean signals in tide gauge records are the astronomical tides. Although a thorough dynamical understanding of ocean tides is very difficult, the basic principles are straightforward. To a very close degree of approximation, tides on the earth are controlled by the moon and the sun. While other heavenly bodies contribute tidal-generating forces, their relative strengths are very small in comparison. Since the motions of the sun and the moon relative to the earth are known very precisely, it is possible to compute the tidal-generating potential to great accuracy at any point on the earth. *Doodson* [1922] was the first to decompose the tidal-generating potential into discrete frequencies and ampli-

Paper number 5B5594.
0148-0227/86/005B-5594$05.00

TABLE 1. Principal Tidal Harmonic Constituents

Name of Tidal Constituent	Symbol	Period, hours	Amplitudes Relative to M_2
Principal lunar	M_2	12.42	1.000
Luni-solar diurnal	K_1	23.93	0.584
Principal solar	S_2	12.00	0.466
Principal lunar diurnal	O_1	25.82	0.415
Principal solar diurnal	P_1	24.07	0.194
Larger lunar elliptic	N_2	12.66	0.192
Lunar fortnightly	M_f	327.86	0.172
Luni-solar semidiurnal	K_2	11.97	0.127
Lunar monthly	M_m	661.30	0.091
Solar semiannual	S_{sa}	2191.43	0.080
Larger lunar elliptic	Q_1	26.87	0.079

tudes. He identified a total of 389 components. The 11 most significant are listed in Table 1. To a close approximation, the tidal generating potential can be described by the seven constituents with largest amplitude. The remaining 382 components have much smaller amplitudes and can usually be ignored.

If the earth were covered by a uniform layer of water, dynamical prediction of the tides at any location would be a simple matter since the period, amplitude, and phase of all tidal constituents are known precisely. However, the presence of continental boundaries and complex bottom topography in nearshore regions and the effects of the earth's rotation make dynamical predictions essentially useless. In practice, the tides at a particular location are determined empirically by harmonic analysis [*Munk and Cartwright*, 1966]. A tide gauge is installed, and measurements are made for a long enough period to resolve the principal constituents (usually a few months to a year or so). The amplitudes and phases of each tidal constituent are then determined by harmonic analysis.

Although the tidal signal can be very large (amplitudes of 1–2 m are common) and can mask other signals in tide gauge records (see Figure 1*a*), they can be predicted very accurately at coastal locations from their harmonic constants. Consequently, the tides can be easily removed from the records. Another method commonly used to reduce tidal signals in the data records is to low-pass filter the time series by numerical filtering with a half-power point around 2 days. Such filtering essentially eliminates the tidal signal from the six largest constituents (see Table 1), as well as many of the smaller amplitude constituents. The effects of such a filtering operation can be seen in Figure 1*b*.

3. Static Inverted Barometer Effects

Another relatively straightforward signal in tide gauge records is the so-called inverted barometer effect of atmospheric pressure. This nondynamical effect results from the downward force on the sea surface due to the mass of the overlying atmosphere. This results not from compression of the water but from a horizontal redistribution of water mass in response to horizontal variations in the sea level pressure (SLP) field. Thus, if SLP changed uniformly over an ocean basin, except for a negligible change due to the small compressibility of seawater, there would be no corresponding change in SLH. Assuming that the total mass of air integrated over an ocean basin remains constant, the change Δh in SLH in response to a change Δp in SLP is given by

$$\Delta h = -\frac{1}{\rho g} \Delta p$$

where ρ is the water density and g is the gravitational acceleration. If Δp is expressed in millibars (mbar) and Δh is expressed in centimeters, the inverted barometer response is -1.01 cm/mbar.

The transient adjustment to a change in SLP is carried out by long gravity waves and is thus very rapid. For example, *Roden* [1965] noted that SLP in San Francisco was the lowest ever recorded on January 27, 1916. Five days later, SLP had risen 60 mbar to the second highest value on record. This rapid and large change in SLP was accompanied by a 53 cm drop in SLH over the same time period.

Robinson [1964] showed through scaling arguments that the open ocean should respond as an inverse barometer to changes in SLP. Since it is a nondynamical effect, there is no net pressure change in the ocean associated with the inverted barometer response. Open ocean inverse barometer response has been demonstrated by *Brown et al.* [1975], who found very low coherence between ocean bottom pressure and atmospheric pressure in the western Atlantic Ocean. *Wunsch* [1972] has also presented evidence for inverse barometer response from 8 years of SLH data at the open ocean island of Bermuda.

Along coastal boundaries, the SLH response to SLP is not so simple. *Robinson* [1964] showed that the response can differ significantly from inverse barometric due to the presence of the coastline. Over a sloping bottom shelf region, SLP can force SLH changes which rapidly propagate with the coast to the right of the direction of propagation in the northern hemisphere (to the left in the southern hemisphere). Thus, for example, along the west coast of North America, the response of SLH to local SLP may be inverse barometric. However, since the spatial scales of SLP are large, there may be additional SLH response propagating poleward from SLP forcing at locations to the south. This propagating response is a dynamical effect of SLP forcing at remote locations.

Attempts to separate local inverted barometer response from other causes of SLH variability have been largely unsuccessful. *Roden* [1966] and *Saur* [1962] both found a strong inverse relationship between SLH and local SLP with a response 1–2 times greater than inverse barometric. The additional response may be due to propagating SLH signals forced by SLP at southerly locations as suggested by *Robinson* [1964]. However, *Saur* [1962] noted that decreases in SLP along the west coast of North America are locally associated with more southerly winds. Similarly, increases in SLP are associated with more northerly winds. This further complicates the problem since alongshore wind stress can also force SLH fluctuations at the coast (see section 5). The SLH response to northerly (southerly) winds is the same sign as the SLH response to an increase (decrease) in SLP. Thus, with the observed coupling between SLP and winds, the responses of SLH to each tend to reinforce, which would cause an apparent response to SLP (if wind effects were not taken into consideration) that would be larger than inverse barometric.

Chelton and Davis [1982] tried to resolve the problem by constructing multiple linear regression models for SLH at 20 locations along the west coast of North America. Both local SLP and wind stress were included as forcing functions as well as atmospheric forcing at locations south of each particular SLH station. The response coefficient for local SLP was still 10–50% larger than inverse barometric.

In spite of the difficulties encountered in verifying a local inverted barometer response to SLP at coastal locations, the second step in analysis of tide gauge records (after removal of

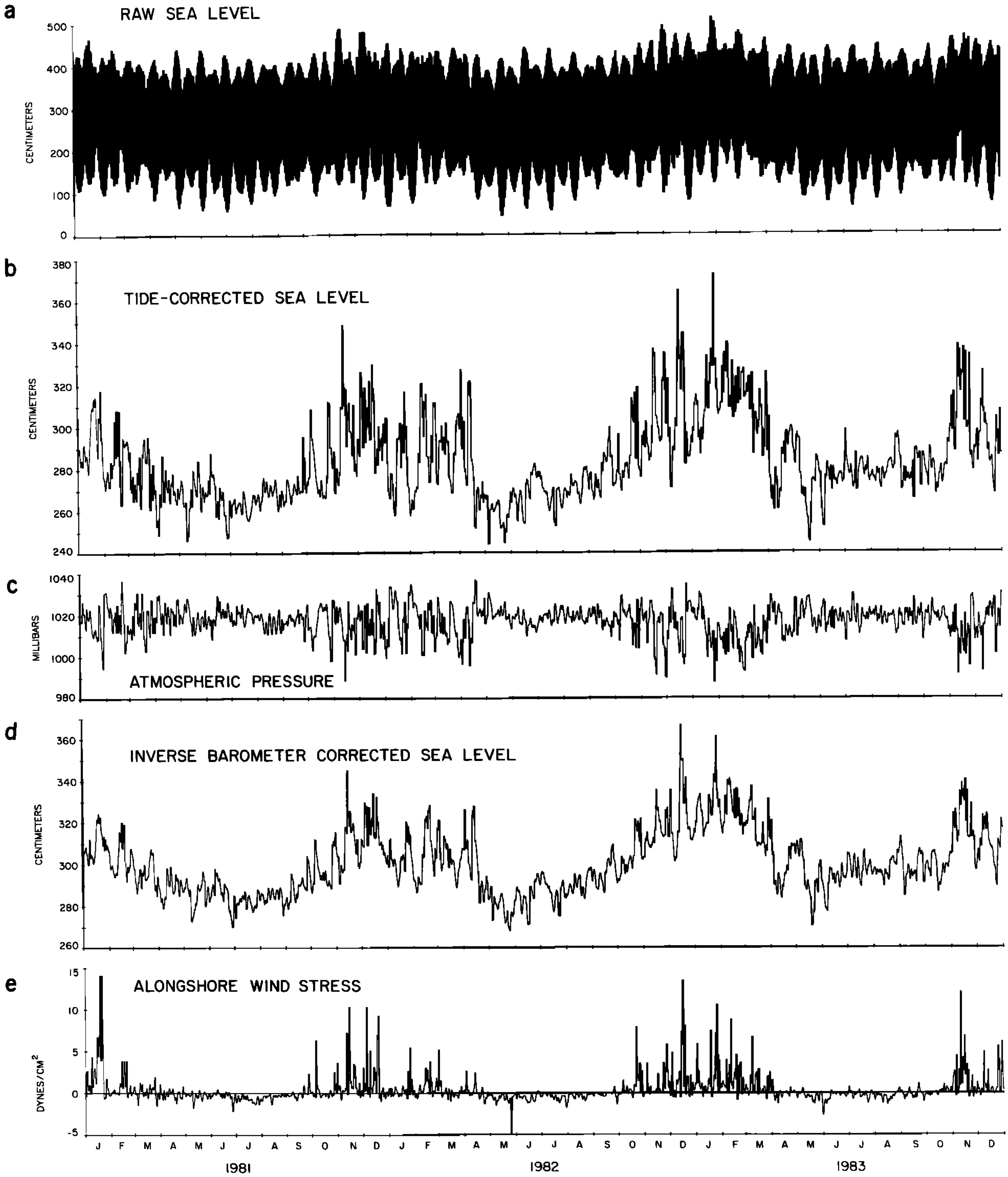

Fig. 1. Time series at Newport, Oregon, for 1981–1983 of (*a*) raw sea level, (*b*) tide-corrected sea level, (*c*) atmospheric pressure, (*d*) inverse barometer corrected sea level, and (*e*) alongshore component of wind stress (positive northward). Note difference in scale in Figure 1*a*.

the astronomical tides; see section 2) is the addition of 1.01 cm for each millibar of SLP change. The argument usually given in defense of this inverse barometer correction procedure is that all past studies have used imperfect winds and that perhaps the apparent nonbarometric response to local SLP would no longer be found if the true winds over the continental shelf were accurately known. In any event, removal of inverted barometer effects typically accounts for 10–15% of SLH variance south of San Francisco and 50–60% of SLH variance to the north [*Chelton and Davis*, 1982]. The inverted barometer SLP effect has a typical value of 1–10 cm (depending primarily on latitude) over daily to weekly time scales.

As an example of the effects of SLP on SLH, time series of tidal corrected SLH and local SLP at Newport, Oregon, are shown in Figures 1*b* and 1*c*. It is easy to visually identify an SLP effect on SLH. Both SLP and SLH variability are strongest during the wintertime from October through April. Most spikes in the sea level record coincide with spikes (of the opposite sign) in the SLP record. Figure 1*d* shows Newport SLH after removing the inverted barometer effect (adding 1.01 cm/mbar). The variance in the residual sea level record is very much reduced, especially in winter when SLP variability is most energetic. There are still a number of spikes in residual sea level. These are generally associated with strong wind events (see section 5).

4. GEOSTROPHIC CURRENTS

Most of the remaining ocean signals in tide gauge records can be attributed to the dynamical effects of geostrophic currents forced by a variety of mechanisms discussed in later sections. Over spatial scales 30 km or more and temporal scales comparable to or longer than the rotational period of the earth, oceanic motions are governed by pressure gradient forces and the Coriolis (or earth rotational) force. Pressure forces also affect more familiar, smaller-scale flows such as in streams and pipes. In these small-scale flows, however, pressure forces are opposed by frictional forces, and both act along the line of flow. In large-scale ocean flows it can be shown through scaling arguments that friction assumes a role of lesser importance (see, for example, *Pond and Pickard* [1978, Chapter 7]), and to a close approximation, the pressure forces are opposed by the Coriolis force. Both forces are perpendicular to the direction of flow. This balance of forces is known as geostrophy.

Suppose that the y axis is aligned in the direction of water motion and the x axis is aligned 90° to the right of the direction of flow. Then the geostrophic balance is

$$fv = \frac{1}{\rho}\frac{\partial p}{\partial x}$$

where p is the total pressure, $\partial p/\partial x$ is the cross-stream pressure gradient, ρ is the water density, v is the water velocity, and $f = 2\Omega \sin \phi$ is the Coriolis acceleration with Ω the rotation rate of the earth and ϕ the latitude. Near the sea surface, the pressure in the water column (after correcting for the inverse barometer effect) is $p = \rho g h$, where h is the sea level measured from a state of rest. Then, assuming that $\partial \rho/\partial x$ is small, the water velocity at the sea surface is

$$v_s = \frac{g}{f}\frac{\partial h}{\partial x}$$

Thus horizontal slopes in SLH are balanced by near-surface flow perpendicular to the SLH gradient. Consequently, surface geostrophic velocity is along contours of constant SLH, and the flow is in a direction such that higher SLH is to the right of the direction of motion in the northern hemisphere and to the left in the southern hemisphere (where the sign of the Coriolis force changes).

It is thus straightforward, in principle, to infer surface flow from maps of SLH. The sea level slopes associated with geostrophic currents are very small. For example, a surface velocity of 2 m/s (which is a rapid flow in the ocean) at 30° latitude is associated with a sea level slope of 74 cm over a distance of 100 km. In other words, the sea surface slope associated with even the strongest currents in the ocean is only about 10^{-5}. The sea level signals associated with the typical 10 cm/s currents along eastern ocean boundaries are about 10 cm over a distance of 200–300 km (i.e., a slope of less than 10^{-6}).

At coastal boundaries, SLH is easily measured by tide gauges. However, open ocean SLH measurements are difficult to obtain in most areas because of a lack of islands on which to install tide gauges. The usual method of estimating SLH in the open ocean is to measure the "steric" sea level computed from the vertical distribution of temperature and salinity. Steric sea level is determined from the hydrostatic equation which, for positive z axis upward, is given by

$$dp/dz = -g\rho(z)$$

Integrating from a reference pressure surface p_0 at depth z_0 to the inverse barometer corrected sea surface z_s where the pressure is zero, gives the steric height of the sea surface relative to z_0,

$$z_s - z_0 = -\frac{1}{g}\int_{p_0}^{0} \alpha \, dp$$

where the specific volume $\alpha = 1/\rho$ is the reciprocal of density, which is a function of temperature, salinity, and, to a lesser extent, pressure. Warm or low-salinity water displaces a larger volume and causes the sea surface to stand higher than cold or high-salinity water. If pressure is measured in units of decibars (dbar), specific volume in units of cm^3/g and the gravitational acceleration is expressed in units of cm/s^2, then steric sea level has units of centimeters. Only in the case where the reference pressure surface p_0 coincides with a "level surface" (a surface of constant gravitational potential) will steric height correspond to the absolute topography of the sea surface. It is generally found that velocities and horizontal pressure gradients in deep water are much smaller than in near-surface waters [e.g., *Reid*, 1961; *Reid and Arthur*, 1975]. That is, pressure surfaces more nearly coincide with level surfaces in deep water. In any case, the steric height only approximates the absolute SLH to the extent that the reference surface is level. *Sturges* [1974] has shown that the relative sea surface topography is not very sensitive to the reference surface chosen, as long as it is deep enough so that water motion is small. In eastern ocean basins, ocean currents are generally slow and relatively shallow and a reference surface between 500 and 1000 dbar (corresponding to water depths of approximately 500 and 1000 m) is adequate. In western ocean basins, ocean currents are stronger and extend to greater depths, and a reference surface of 2000 dbar or deeper (corresponding to water depths 2000 m or deeper) is required.

Note that the geostrophic relation is a steady state balance of forces. Thus geostrophy can only truly exist for time independent flow. Yet the ocean circulation changes over a wide range of time scales. From theoretical considerations, geostrophic adjustment to changes in the pressure field occurs rather quickly [*Blumen*, 1972] so that steric height accurately represents variations in the flow over time scales longer than a few days. Steric height is thus useful for mapping the long-term average flow at the sea surface. Figure 2 shows the average steric height in the Pacific Ocean computed from over 100 years of ship measurements of temperature and salinity in the upper 1000 m. The reference level used in this map is 1000 dbar. Use of a deeper reference level would alter the relative sea surface topography somewhat, but the salient features would remain the same.

All of the well-known general features of the circulation and associated SLH are evident in Figure 2. In the northern hemisphere, the highest SLH (approximately 220 cm) is in the western subtropical Pacific (25°N, 125°E) and the lowest SLH (approximately 100 cm) is in the western subpolar Pacific (50°N, 165°E). Since geostrophic flow is along contours of constant

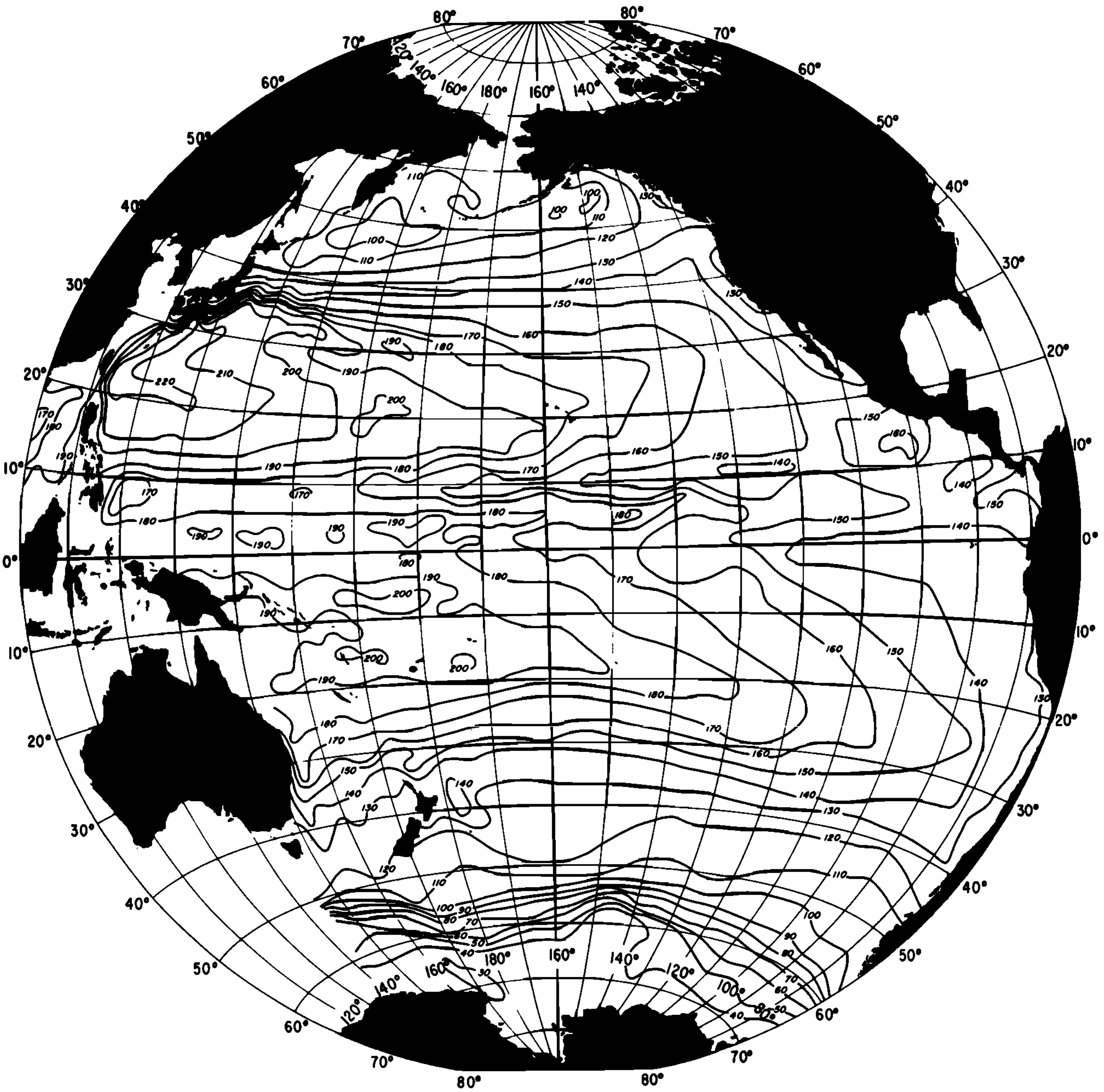

Fig. 2. Steric height (in centimeters) relative to 1000 dbar for the Pacific Ocean [from *Wyrtki*, 1974]. The contribution from a "standard ocean" of uniform salinity (35 ppt) and uniform temperature (0°C) has been removed prior to contouring.

SLH, this implies a clockwise circulation at low to mid-latitudes (the subtropical gyre) and counterclockwise circulation at mid- to high latitudes (the subpolar gyre). The speed of geostrophic flow is strongest in the western Pacific where horizontal gradients of SLH are most intense. Along the west coast of North America where SLH gradients are small, the geostrophic currents are weak with equatorward flow south of 50°N and poleward flow to the north.

In the southern hemisphere the highest SLH (approximately 200 cm) is in the western subtropical Pacific (15°S, 170°W). Thus, in subtropical regions the flow is counterclockwise. This circulation is similar to the subtropical gyre in the northern hemisphere, but the sense of the flow is reversed (due to the change in sign of the Coriolis acceleration in the southern hemisphere). There is no southern hemisphere subpolar gyre due to the fact that no land masses impede the flow at high southern latitudes. The lowest SLH (approximately 40 cm) is in the southern polar region close to the coast of Antarctica along latitude 65°S. This results in a strong flow from west to east around the Antarctic continent in all ocean basins (the Antarctic Circumpolar Current).

The SLH pattern and associated geostrophic flow in the Atlantic Ocean shows the same general features as the Pacific Ocean SLH shown in Figure 2 (see, for example, *Stommel et al.* [1978]). There are subtropical gyres in both hemispheres with strong poleward flow in the west and weak equatorward flow in the east. There is a subpolar gyre in the northern hemisphere and the Antarctic Circumpolar Current in the southern hemisphere.

The average steric height shown in Figure 2 portrays a useful picture of the long-term average circulation. However, it is known that this average circulation varies temporally so

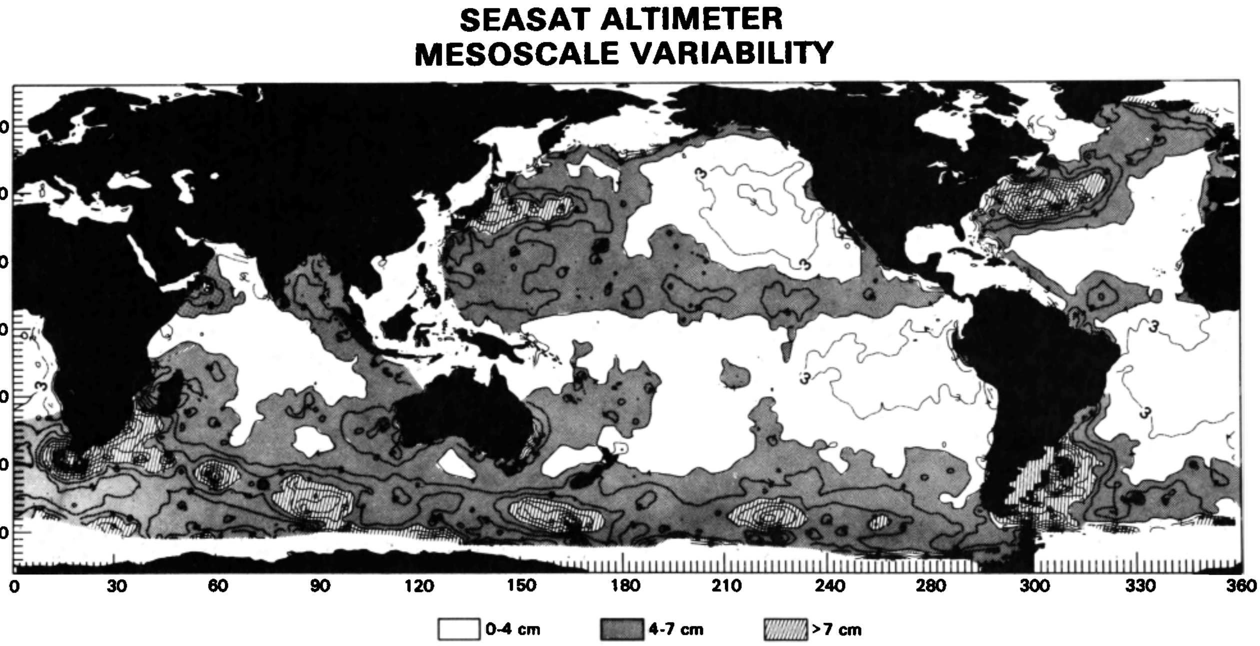

Fig. 3. Global root mean square mesoscale sea level variability for a 25-day period in early fall of 1978 as measured by the Seasat altimeter [from *Cheney et al.*, 1983].

that at any particular time, SLH will not look identical to that shown in Figure 2. The distribution of ship observations of temperature and salinity is not adequate to resolve temporal variability of the flow except over very long time scales (see, for example, *White and Hasanuma* [1980] and *Chelton et al.* [1982]). Recent technological advances in satellite altimetry allow measurement of sea level to a precision of about 5 cm from a satellite orbiting at a height of 800 km above the sea surface [*Tapley et al.*, 1982]. Much of this SLH signal represents spatial variations in the geoid from gravitational effects and is therefore not oceanographic [*Marsh and Martin*, 1982]. The geoid effects are time invariant and can thus be easily removed by examining differences in SLH from one orbit time to another.

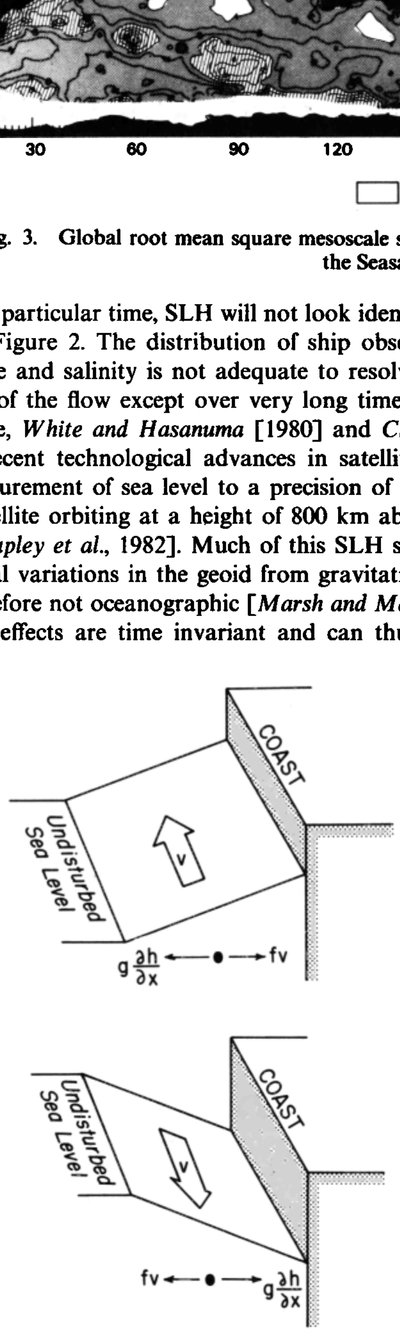

Fig. 4. Schematic diagram of relation between sea level and geostrophic velocity along an eastern ocean boundary in the northern hemisphere.

Cheney et al. [1983] have used this method to map the global variability of SLH over a 1-month period in the fall of 1978 (Figure 3). The rms variations over this period range from 1–2 cm in mid-ocean regions to 40 cm in the major current systems. These variations in SLH can be caused by meandering of the currents, shedding of eddies, or changes in the speed of the surface flow. *Fu and Chelton* [1984, 1985] have recently used altimeter data to study large-scale, low-frequency changes in sea surface topography and related geostrophic velocity in the Antarctic Circumpolar Current between 45°S and 65°S. The use of satellite altimetry to study surface geostrophic currents is relatively new. The technique promises to reveal exciting new aspects of variations in surface ocean circulation using the next-generation radar altimeter (call TOPEX) with an expected launch in 1990.

For interpretation of SLH signals in tide gauge records it is instructive to consider the effects of nearshore geostrophic currents on coastal sea level. As shown in Figure 4, poleward flow along the west coast of North America results in a rise of SLH from west to east. Correspondingly, equatorward flow results in a drop in SLH from west to east. The SLH slope is proportional to the geostrophic velocity. Thus a tide gauge at the coast would indicate a rise in SLH when poleward flow increases (or equatorward flow decreases) and a drop in SLH when poleward flow decreases (or equatorward flow increases).

5. Coastal Upwelling

Examination of residual SLH after correcting for the inverted barometer effect of SLP reveals frequent large positive and negative fluctuations with typical time scales of 2–10 days. Examples can be clearly seen in the Newport tide gauge data shown in Figure 1*d*. The 2- to 10-day duration is the typical time scale of synoptic wind events associated with traveling atmospheric pressure systems. On theoretical grounds there is a strong basis to expect that SLH responds to local wind forcing. Over very short time scales or in semienclosed basins,

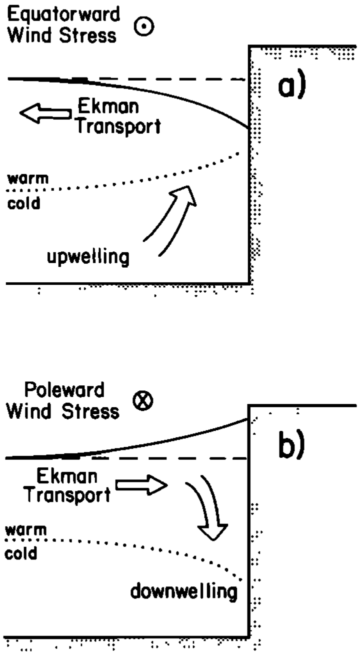

Fig. 5. Schematic diagram of (*a*) coastal upwelling and (*b*) coastal downwelling response to alongshore winds along an eastern ocean boundary in the northern hemisphere.

onshore winds can "pile up" water against the coast. However, over longer time scales and along an open coastline, the effects of the earth's rotation tend to make onshore winds relatively unimportant compared with the alongshore component. Indeed, comparison of SLP corrected SLH with local alongshore winds in Figures 1*d* and 1*e* shows that many of the stronger SLH signals coincide with strong alongshore wind events.

The dynamical effects of wind stress at the sea surface were first explained by *Ekman* [1905]. He showed that the Coriolis force from the earth's rotation and frictional forces in the upper ocean result in a net vertically integrated transport of water 90° to the right of the wind in the northern hemisphere (90° to the left in the southern hemisphere). The actual water velocity decays exponentially and rotates clockwise with depth in the northern hemisphere (counterclockwise in the southern hemisphere). Thus most of the total Ekman transport is concentrated in the very near surface region (upper 50 km).

Winds blowing from the north along the west coast of North America thus result in an offshore transport in the surface waters. To conserve mass, this divergence of relatively warm surface water must be compensated by a vertical transport of colder subsurface water at the coast, the classical picture of coastal upwelling (Figure 5*a*). Since the newly upwelled water is colder and more dense, it displaces a lesser volume than the original warm water present prior to upwelling. Consequently, SLH at the coast drops in response to equatorward winds.

In a similar manner, the Ekman transport associated with poleward winds along the west coast of North America results in a net onshore transport in the surface waters. This must be compensated by downwelling at the coast (Figure 5*b*). The resulting accumulation of a thick layer of warm, less dense water at the coast leads to a rise in SLH.

The nearshore ocean responds to the sea surface slopes induced by coastal upwelling by forming geostrophic alongshore currents as in Figure 4. The response to equatorward (poleward) wind stress is equatorward (poleward) geostrophic flow at the sea surface. Thus, while the wind and surface velocity are in the same direction, the coupling is not from direct frictional effects of winds "dragging" the water in the direction of the wind. Rather, the coupling is through Ekman transport and subsequent geostrophic adjustment induced by rotation of the earth.

The above picture is an overly simplistic view of the complex dynamics which take place during coastal upwelling and downwelling. For example, during coastal upwelling, cold water accumulates rather quickly in the surface region near the coast. Continued upwelling then transports this cold water offshore by Ekman dynamics. Since this offshore transport is restricted to the near-surface region, this eventually leads to cold water overlying warmer subsurface water. In this unstable situation, mixing must occur. These and other aspects of the detailed dynamics of coastal upwelling are discussed by *de Szoeke and Richman* [1981, 1984].

Nonetheless, the simple explanation presented here can account qualitatively for many of the SLH events in Figure 1*d*. For example, a number of strong positive SLH events can be associated with strong poleward wind events. Similarly, many negative SLH events coincide with equatorward wind events. Typical magnitudes of SLH response to wind forcing are 10–20 cm. Careful study of Figures 1*d* and 1*e* reveals a number of SLH events without corresponding wind events. There are also examples of wind events with no apparent SLH response. It therefore appears that the local response to winds is not the only important cause of SLH variability over these time scales. Furthermore, the amount of SLH change in response to upwelling or downwelling clearly depends on the stratification. Since stratification varies on seasonal and longer time scales, it is difficult to quantify the SLH response to a given wind stress. It is thus apparently not a simple matter to remove the SLH response to local winds from tide gauge records. An approximate solution is to construct a regression model to determine in a statistical sense the transfer function between wind and SLH.

6. COASTAL TRAPPED WAVES

Part of the discrepancy between SLH and local wind events evident in Figures 1*d* and 1*e* is due to the fact that not all SLH fluctuations are locally forced. This has been alluded to in section 3 where it was noted that SLP can force SLH variations which propagate along coastal boundaries. In a similar manner, alongshore wind stress can force coastally trapped propagating SLH variations. *Adams and Buchwald* [1969] and *Gill and Schumann* [1974] have shown through scaling arguments that wind stress is one to two orders of magnitude more effective than SLP in forcing coastally trapped waves.

The propagation of SLH disturbances along the coast can be qualitatively understood by analogy with a rock dropped in a pond of water. The momentary disruption of the water level propagates radially outward in the form of gravity waves. For larger-scale disturbances such as those forced by winds at the coast, the effects of the earth's rotation become important. The SLH signals propagate away from the region of forcing using the coastline as a waveguide. Due to the Coriolis force on large-scale motions, the direction of propagation is such that the coastline is to the right in the northern hemisphere and to the left in the southern hemisphere.

The dynamics of coastally trapped waves have been dis-

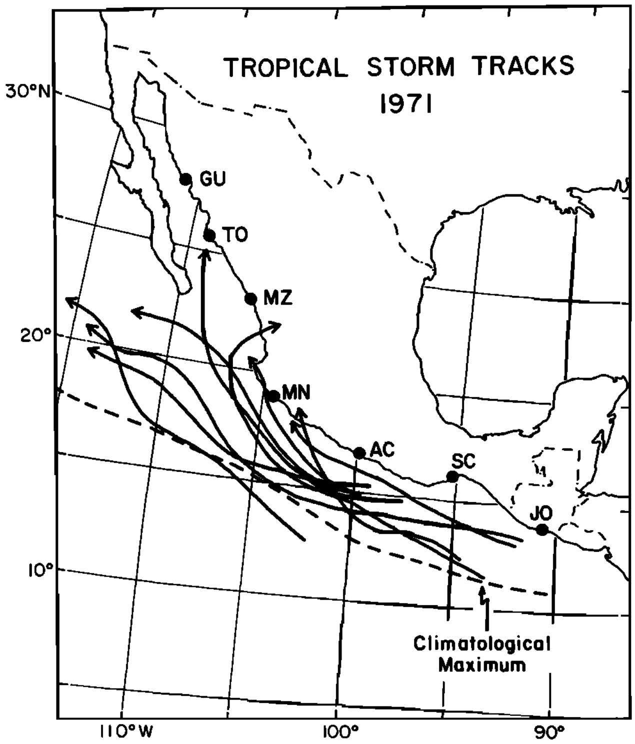

Fig. 6. Tropical storm tracks along the coast of Mexico during 1971. The sea level stations labeled are GU, Guaymas; TO, Topolobampo; MZ, Mazatlan; MN, Manzanillo; AC, Acapulco; SZ, Santa Cruz; JO, San Jose [from *Enfield and Allen*, 1983].

cussed by *Clarke* [1977], who developed a linearized model which includes the effects of vertical stratification in the water column and cross-shore variations in the bottom topography. Alongshore winds at the coast generate SLH fluctuations which propagate poleward along eastern ocean boundaries. In the region of direct forcing, the nature of the SLH signal can be quite complex, depending on the propagating characteristics of the wind forcing. However, once the forcing ceases or the SLH signal propagates out of the forcing region, SLH variability consists of a superposition of free wave modes. If the variability is dominated by a single mode, the SLH signal propagates as a simple wave form with phase speed appropriate for that mode. It is generally found that the SLH variability associated with coastal-trapped waves is dominated by the first-order mode which has a phase speed of 100–300 km/d. Of course, in the real ocean, frictional forces and alongshore variations in stratification and bottom topography alter the shape and propagation speed of coastal-trapped waves.

The existence of wind-forced coastal-trapped waves has been nicely demonstrated by *Enfield and Allen* [1983]. They examined SLH at the seven stations along the coast of Mexico shown in Figure 6. From May to October 1971, nine major positive SLH events with 10–20 cm amplitude were observed at all stations from southern Mexico to the northern region of the Gulf of California (Figure 7). The time of occurrence of each SLH signal at the seven stations is progressively later from south to north, suggesting poleward propagation of SLH disturbances. These signals are typical of those observed every summer in this region (see, for example, *Christensen et al.* [1983]). For 1971, each major SLH signal can be associated with the occurrence of a major tropical storm. These storms form in the eastern tropical Pacific and usually move northwestward parallel to the Mexican coast at 400–600 km/d to as far north as 20°N (Figure 6), then turn westward into the open Pacific Ocean and decrease in intensity. The winds circulate counterclockwise around the storm centers that lie offshore. Thus the winds over the coastal zone generally blow northward.

In response to these downwelling-favorable winds, SLH rises as expected from the discussion of section 5. Equatorward of 20°N, the SLH signals propagate along the coast with phase speeds which differ from one event to another. These phase speeds (400–500 km/d) closely match the propagation speeds of the storms in this region. Poleward of 20°N (where the storm tracks generally turn westward) the SLH signals continue to propagate along the coast. The phase speeds are significantly reduced (220–320 km/d), and there is smaller variance in propagation speed from one event to another. In this region the waves propagate freely, and their characteristics depend only on the ocean bottom topography and the stratification in the water column.

This example is strong evidence for the generation and propagation of coastal trapped waves along eastern ocean boundaries. Other examples have been given by *Clarke* [1977] and *Wang and Mooers* [1977] for the California coast and by *Smith* [1978] for the Peru coast. Coastal-trapped waves have also been observed propagating equatorward along western ocean boundaries [e.g., *Mysak and Hamon*, 1969; *Brooks and Mooers*, 1977]. It is thus evident that an SLH signal observed at any particular tide gauge may have been generated by atmospheric forcing at remote locations. Consequently, it is generally unwise to consider only local forcing when attempting to isolate the cause of SLH variability in tide gauge records.

Although models of coastal-trapped waves can account qualitatively for propagating signals, it is not possible to use the models for prediction of the amplitude of the SLH signal as it propagates. For example, *Halliwell and Allen* [1984] attempted to predict SLH variability along the west coast of the United States using the coastal-trapped wave theory discussed above. In some cases, their predictions agreed favorably with observed SLH variability. In other cases, the predicted amplitude of SLH differed from observed SLH. The discrepancy is due in part to simplified assumptions in the theory. But even if the theory were perfect, it is not practical to quantitatively predict SLH since it is impossible to obtain the necessary measurements of water density along the propagation path. The density structure varies both spatially and temporally, and these variations alter the structure and phase speed of the coastal-trapped wave modes. Thus, while the existence of forced and freely propagating coastal-trapped waves is relatively easy to understand dynamically, the SLH amplitudes and propagation speeds cannot be predicted in a quantitative sense.

Since the time scales of propagating SLH events are typically 2–10 days, the presence of these ocean signals in tide gauge records can be greatly reduced by low-pass filtering the data. One form of filtering is to construct simple monthly averages of the data. A better approach which results in less contamination from high frequencies is to apply a more sophisticated filter which has smaller side lobes in the frequency domain. One can then extract monthly averages from the filtered residuals, if desired. The residual SLH signals remaining in the low-pass-filtered tide gauge data are discussed in the next four sections.

7. SEASONAL VARIABILITY

The dominant signal in time series of low-frequency SLH is generally the seasonal cycle. Seasonal variability is even evi-

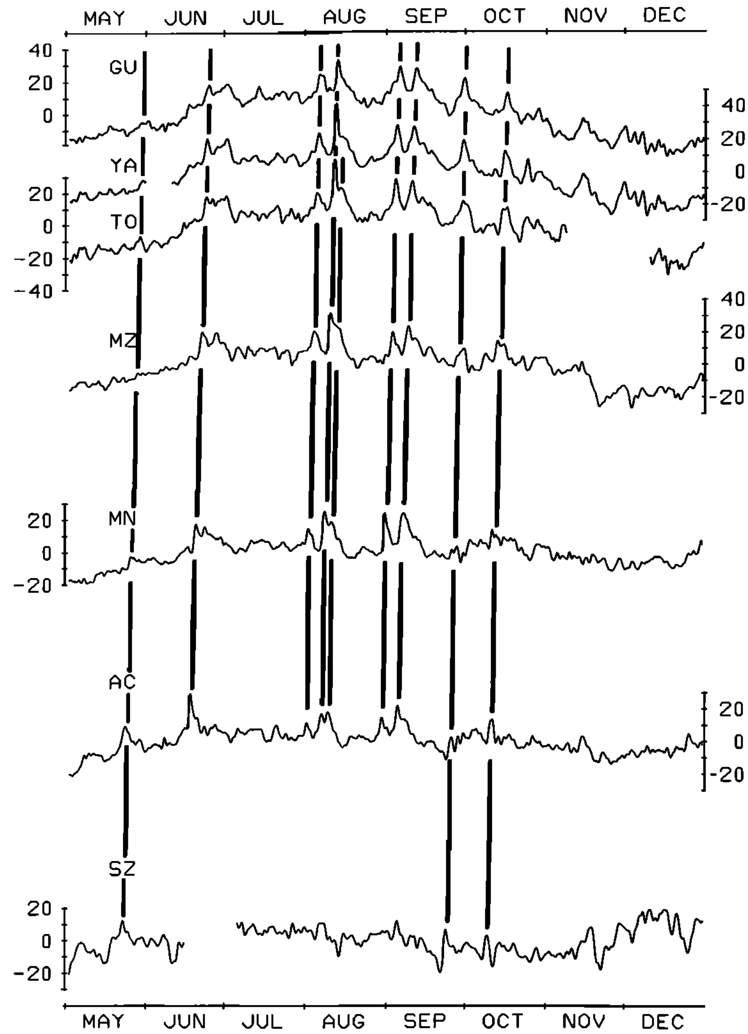

Fig. 7. Low-pass-filtered sea level at the seven stations shown in Figure 6 for summer and fall of 1971. Time series are vertically spaced in proportion to the station separations. Straight lines indicate propagating events associated with the tropical storms shown in Figure 6 [from *Enfield and Allen*, 1983].

dent in tidal- and inverse barometer-corrected SLH records such as that shown in Figure 1*d*. *Pattullo et al.* [1955] have presented a global summary of the seasonal variability of SLH. The amplitude and nature of the seasonal cycle vary with geographical location. The peak-to-peak amplitude of seasonal SLH variability ranges from a few centimeters at low latitudes to 20–40 cm at high latitudes. The seasonal variability generally has an annual period, but at some locations there is also a strong semiannual component.

Three examples of seasonal SLH variability (after removing the inverted barometer effects of SLP) along the eastern boundary of the Pacific Ocean are shown in Figure 8. They demonstrate the seasonal influence of steric variations (density changes) and wind forcing and show that the amplitudes and phases of seasonal variability vary from one region to another. At Acapulco the seasonal cycle is relatively strong (approximately 20 cm range) and is in phase with the annual heating and cooling cycle; highest SLH occurs in July and August, and lowest SLH occurs in March. The flattening of the curve during November, December, and January is an indication of the presence of a semiannual component in the seasonal cycle. In contrast, the seasonal cycle of SLH at Newport is very strong (approximately 25 cm range), is almost purely annual, and is about 180° out of phase with the annual heating and cooling cycle; highest SLH occurs in December, and lowest SLH occurs in June and July. At Talara there is very little seasonal variability of SLH (only a 4-cm range), though this is not always the case at low latitudes. For example, seasonal SLH variability is much larger at Buenaventura, Columbia (4°N), and Balboa, Panama (9°N), only a short distance north of Talara [see *Enfield and Allen*, 1980]. This is due to wind forcing from a strong monsoonal cycle in the atmospheric circulation of the Panama Bight in the eastern tropical Pacific.

There are a number of causes for seasonal variations in SLH. The most obvious is seasonal variations in the thermal structure of the upper ocean from heating and cooling associated with seasonal changes in solar insolation. *Montgomery* [1938] was the first to attempt to quantify the relation between SLH and thermal effects. He noted that the seasonal change in surface temperature from 8°C in February to 18°C in July at Charleston, South Carolina, could account for the observed seasonal 19-cm SLH increase at that location if these thermal effects extended to a depth of 100 m.

While thermal heating could account for the observed seasonal variability of SLH at Acapulco (Figure 8), it cannot explain the seasonal cycle at Newport, where the highest SLH occurs in winter. As noted by *Reid and Mantyla* [1976], seasonal heating and cooling effects in this region are small relative to the effects of nearshore geostrophic currents in causing changes in SLH. Off the Oregon coast, the flow is strong and

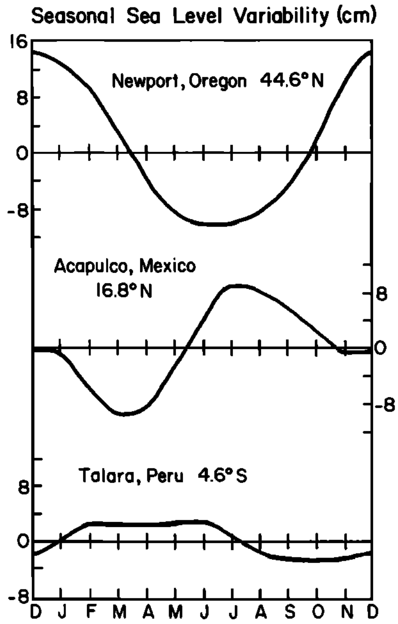

Fig. 8. Seasonal cycles of sea level at three stations along the eastern boundary of the Pacific Ocean.

equatorward in summer when the equatorward wind stress is strongest (Figure 1*e*) and poleward or weakly equatorward in winter when nearshore winds are poleward. As discussed previously (section 4), this seasonal variation in geostrophic velocity results in highest coastal SLH in winter and lowest coastal SLH in summer (Figure 4). This is conspicuously out of phase with the heating and cooling cycle and can explain the seasonal behavior of SLH at Newport (Figure 8).

There are other mechanisms which can influence seasonal variability of SLH, but they generally are of less importance than geostrophic currents and thermal heating and cooling. For example, at some locations the freshwater effects of river inflow alter the density of the near-surface waters, thereby affecting the seasonal variability of SLH. *Meade and Emery* [1971] showed that river runoff is important at a number of stations along the east coast of the United States. Salinity effects on SLH have also been shown to be important to nearshore SLH in the Gulf of Alaska [*Royer*, 1979, 1981].

To remove the seasonal cycle and thus enhance other sources of SLH variability, it is not essential to understand the cause of the seasonal change in SLH. If a truly seasonally recurring phenomenon exists in the data record, it can be easily computed and removed. The two methods most commonly used to define the seasonal cycle are either to (1) compute the long-term average separately for each calendar month, or (2) determine the annual and semiannual components of variability by harmonic analysis. It is generally found that the two methods give virtually the same results as long as the data record spans at least several seasonal cycles. Using either method to define the seasonal cycle, the residual SLH remaining after subtracting the seasonal values from observed monthly averages is called anomalous SLH. The following two sections discuss oceanographic causes for variability of anomalous SLH.

8. LOW-FREQUENCY ATMOSPHERIC FORCING

Construction of monthly averages and removal of the seasonal cycle greatly reduces the variability in SLH records. Anomalous (nonseasonal) variations in the mechanisms which influence seasonal variability of SLH (see section 7) can also cause anomalous variations in SLH. *Enfield and Allen* [1980] and *Chelton and Davis* [1982] have thoroughly analyzed monthly SLH anomalies along the eastern boundary of the Pacific to determine the causes of residual variability. To illustrate characteristics typical of monthly anomaly SLH, time series for 19 stations along the eastern boundary of the Pacific are displayed in Figure 9. The standard deviations at these locations after correcting for the inverted barometer effect range from 4 to 7 cm. Although the SLH fluctuations are small, their large spatial coherence (Figure 9) is rather clear evidence that the signals are real and not merely noise or errors in measurement.

The large-scale coherence of anomalous SLH variability has been quantified by *Chelton and Davis* [1982] using what has been called empirical orthogonal function (EOF) analysis in meteorology and physical oceanography (see *Davis* [1976] for a summary of the technique which is essentially equivalent to principal component analysis). EOFs provide a modal decomposition of variability at a number of different spatial locations, much like Fourier analysis in the wave number domain. The virtue of EOFs is that they provide the most efficient representation in a least squares sense [see *Davis*, 1976]. Approximately 40% of the variability over 20 stations from southern Mexico to the Aleutian Islands consists of a general rise or fall in SLH. The amplitude of this large-scale response is remarkably constant from Mexico to Alaska with typical values ranging from a few centimeters to 10–20 cm for some of the stronger events.

In an attempt to identify the causes of these monthly SLH anomalies, *Chelton and Davis* [1982] constructed multivariate regression models at each station. Much of the high-frequency (periods less than 1 year) aspects of anomalous SLH variability appears to be related to large-scale monthly anomalies in the wind field over the North Pacific Ocean. The SLH response is consistent with that expected from the discussion in section 5; poleward wind anomalies along the west coast of North America result in positive SLH anomalies. Similarly, the response to equatorward wind anomalies is a decrease in SLH.

Using multivariate regression models, it is a simple mater to remove the effects of low-frequency atmospheric forcing from time series of monthly anomaly SLH. This approach reduces the anomalous SLH variability by 5–15% south of San Francisco and 20–40% at stations to the north [see *Chelton and Davis*, 1982, Table 4].

Before turning to the cause of most of the remaining anomalous SLH variability, we pause to point out a nonoceanographic signal in tide gauge records which makes analysis of atmospheric effects on SLH difficult. At three Aleutian Island stations (Attu, Adak, and Unalaska), there are instances of apparent sudden tidal datum level changes followed by a gradual return to normal over a period of several years (Figure 10). In particular, there is a shift of about 20 cm at Attu in 1965 and shifts of about 15 cm at Adak and Unalaska in 1957. *Wahr and Wyss* [1980] have related these signals to vertical crustal motion associated with the major Aleutian earthquakes of 1957 and 1965. From an oceanographic perspective these signals are an unwanted noise that introduce nonoceanographic variability in the data records. Indeed, they are largely responsible for the rather poor performance of the regression models constructed for these stations. For example, atmospheric forcing accounts for less than 10% of the SLH variability at Attu and Adak.

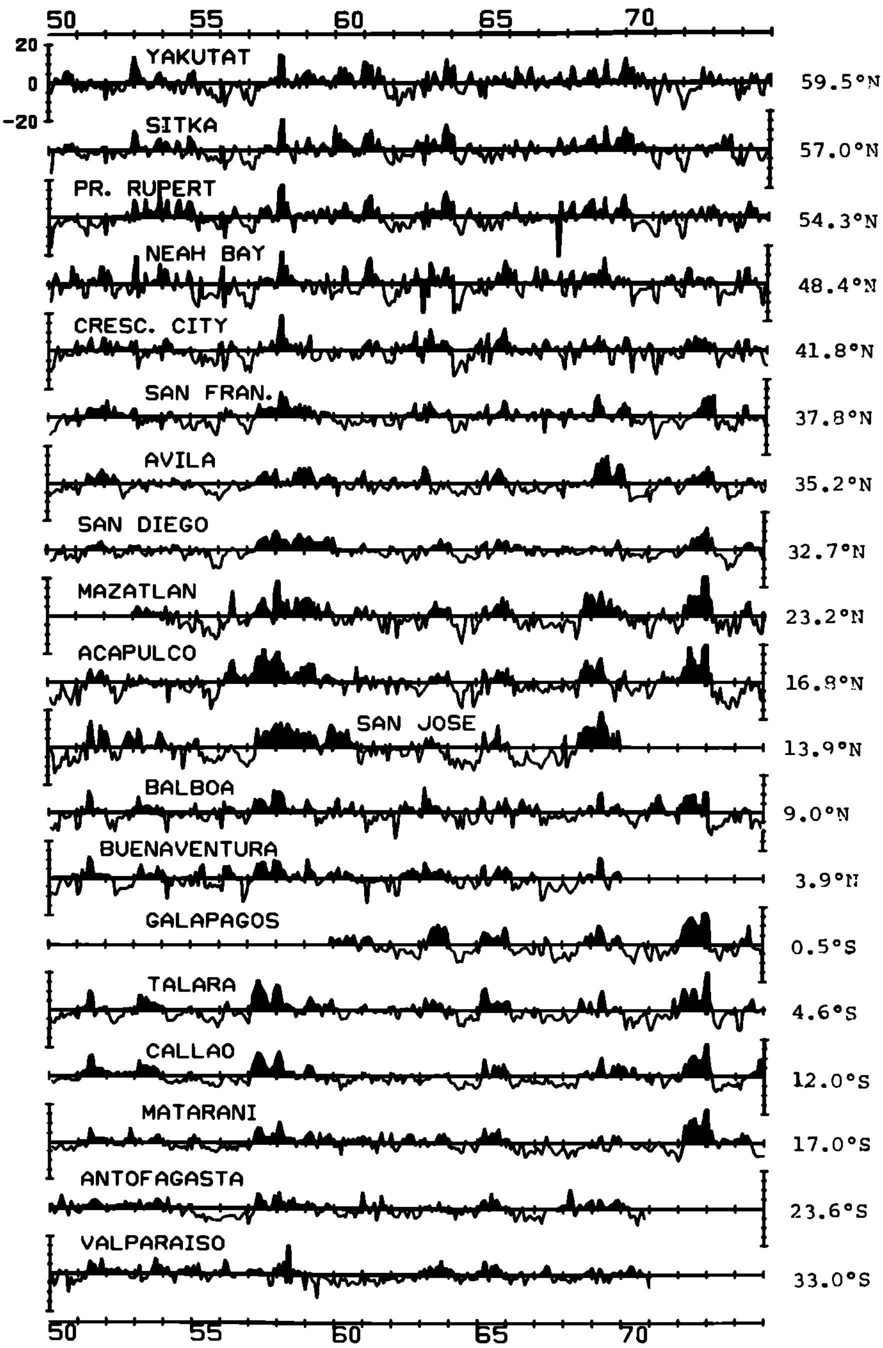

Fig. 9. Time series of monthly average sea level anomalies from 1950 through 1974 at 19 stations along the eastern boundary of the Pacific [from *Enfield and Allen*, 1980].

9. EL NIÑO EFFECTS

The atmospheric effects discussed in the preceding section account for less than half of the variability in the anomalous SLH records. Examination of frequency spectra reveals that most of the remaining variability consists of low-frequency, interannual (periods longer than a year) energy. As an example, the autospectrum of anomalous SLH at San Francisco is shown by the solid circles in Figure 11. The variability is dominated by energy at the lowest frequencies. For comparison, the open circles in Figure 11 correspond to the autospectrum of anomalous alongshore wind stress at San Francisco. It is apparent that the characteristic time scales of atmospheric variability in monthly anomalies are different from those of SLH. The wind field shows a more nearly uniform distribution of energy with frequency.

The mismatch in time scales between SLH and atmospheric forcing apparent from Figure 11 suggests that most of the low-frequency SLH variability must be of oceanic origin. From the discussion of section 6 it might be expected that the nature of this oceanic variability could be in the form of coastally trapped propagating SLH signals from the south. It is well known that oceanic variability in the tropical Pacific is dominated by the El Niño phenomenon which has time scales of 3–7 years. Recent reviews of the present state of knowledge about El Niño can be found in the works by *Rasmusson and Carpenter* [1982], *Philander* [1983], and *Cane* [1983]. In order to establish a framework in which to understand the

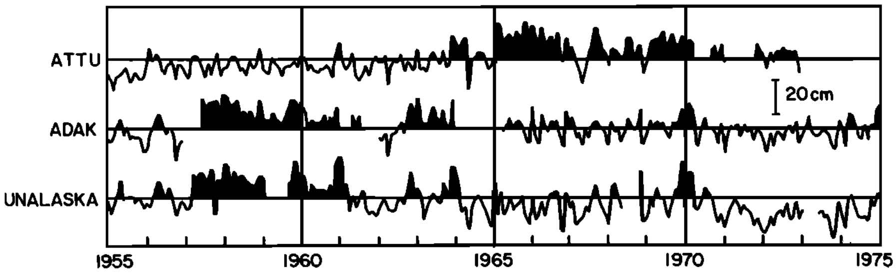

Fig. 10. Time series of monthly average sea level anomalies at three stations in the Aleutian Islands.

influence of El Niño on SLH, we include here a brief summary of the features common to most El Niño events during the past 30 years.

Definitions of El Niño vary, but the phenomenon is usually associated with a rapid appearance of an unusually thick, warm layer of water off the coast of Peru and southern Ecuador. The steric effects of this warm water result in a large increase in SLH. *Rasmusson and Carpenter* [1982] have recently presented a composite picture of atmospheric wind and sea surface temperature (SST) anomalies associated with El Niño based on six events between 1949 and 1976. In this composite picture the "typical" El Niño is preceded by at least 18 months of anomalous strong westward trade winds in the western and central equatorial Pacific. This westward wind forcing in the equatorial regions (where the Coriolis force is small) "pushes" water to the west, resulting in higher sea level in the west and lower sea level in the east. This sea level tilt is associated with a warming of the surface water in the west and cooling of surface waters east of 160°E.

In a typical development the normally westward trade winds weaken and sometimes actually reverse along the equator west of the dateline in September or October of the year preceding an El Niño. The response to this weakening of the trade winds is a relaxation of the zonal sea level slope along the equator. The drop in sea level in the western tropical

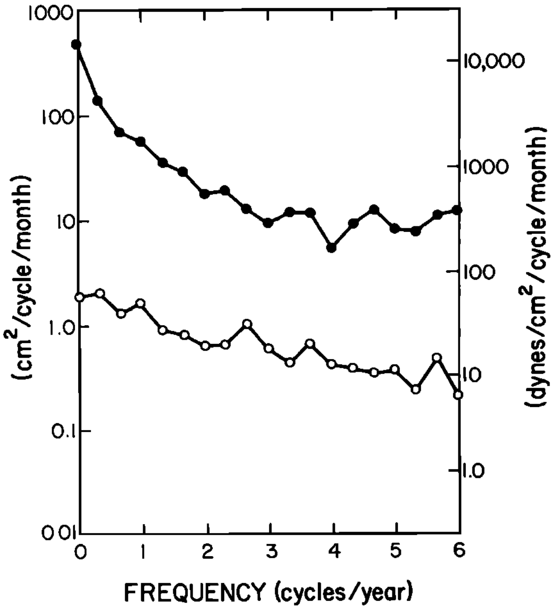

Fig. 11. Frequency spectra of monthly average inverse barometer-corrected sea level (solid circles) and wind stress (open circles) at San Francisco. Seasonal cycles have been removed. Spectral estimates are based on approximately 30 degrees of freedom.

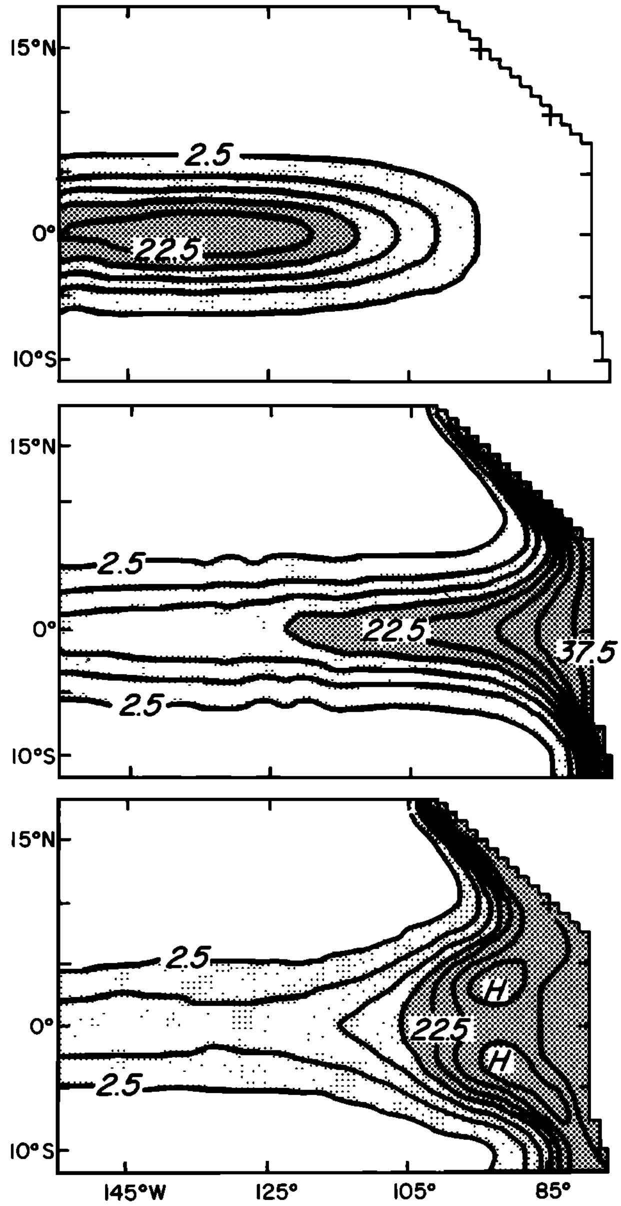

Fig. 12. Numerical model simulation of a freely propagating linear, equatorially trapped wave impinging on the eastern boundary of the Pacific Ocean. The contours represent the interface depth (in meters) in a two-layer model. Because the sea surface responds as a mirror image of the interface depth (but with reduced amplitude) in a two-layer model, these contours may be thought of as SLH approximately in units of centimeters. This sea level signal was forced by an easterly wind anomaly west of 170°W in the tropical Pacific one month prior to the top panel. The middle and lower panels show the sea level signal 2 and 3 months following the wind event (from *Enfield* [1981] after *O'Brien et al.* [1981]).

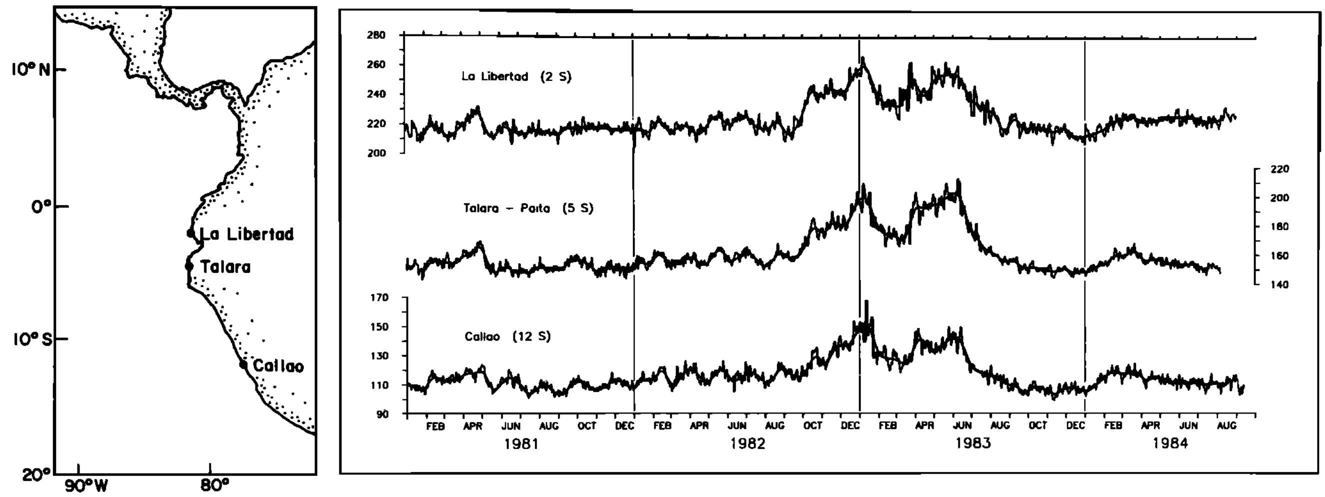

Fig. 13. Sea level (in centimeters) during 1981–1984 at three stations along the coast of South America. Both the raw data (corrected for tides and the inverted barometer effect and low-pass filtered with a half power point at 2 days) and low-pass-filtered data (half power point at 30 days) are shown for each station.

Pacific propagates eastward as a very long wavelength equatorially trapped wave and reaches the South American Coast about 2 months later in late December or early January. The arrival of the equatorially trapped wave at the eastern boundary of the tropical Pacific triggers a warming of the surface waters off the coasts of Peru and Ecuador and a corresponding rise in SLH which signals the onset of El Niño.

The most recent occurrence of El Niño was in 1982. Detailed descriptions of meteorological and oceanographic aspects of this event (probably the most thoroughly documented) can be found in the works by *Philander* [1983] and *Cane* [1983]. The 1982 event differed in several respects from the typical El Niño described above. The initial weakening of the westward trade winds occurred in June–July rather than the usual September–October. The precursors of the typical El Niño did not occur; the trade winds were not unusually strong prior to the weakening, and SST was not anomalously high in the western equatorial regions or low in the east. Warm water and high SLH appeared rather suddenly along the coast of Peru in early fall of 1982, approximately 2 months after initial weakening of the trade winds in the western tropical Pacific.

In summary, it appears that timing relative to the seasonal cycle is a common but not an essential element of El Niño. A feature common to all El Niño events over the past 30 years is a significant weakening of the trade winds in the western tropical Pacific about 2 months prior to the appearance of warm water off the coast of Peru. Analytical and numerical models of ocean response to such a weakening of the trade winds can reproduce many of the observed features in SST and SLH [*McCreary*, 1976; *Hurlburt et al.*, 1976; *Busalacchi and O'Brien*, 1981; *Schopf and Harrison*, 1983].

The response of a linear two-layer model ocean to a eastward wind anomaly (equivalent to a weakening of westward trade winds) west of 170°E in the tropical Pacific is shown in Figure 12. The contours represent the depth of the interface between the two layers at time lags of 1, 2, and 3 months after initiation of the wind anomaly. In a two-layer model, SLH responds as a mirror image of the interface depth but with reduced amplitude. That is, a deepening of the interface corresponds to a rise in SLH. Thus the contours of interface depth in Figure 12 can be thought of as contours of SLH, with an appropriate scaling factor which depends only on the density difference between the two layers in the model. The model response is a positive SLH anomaly which propagates eastward along the equator (top panel) and reaches the eastern boundary of the tropical Pacific about 2 months after initiation of the wind anomaly (middle panel). The response along the eastern boundary is an increase in coastal SLH. The spatial structure and timing of the model SLH signal agree very favorably with observed values [*Wyrtki*, 1977, 1979, 1985]. As discussed in section 6, an anomalous SLH signal along the eastern boundary of the Pacific propagates poleward in both hemispheres in the form of coastal-trapped waves (middle and lower panels). The amplitude of the SLH anomaly decreases near the equator as the disturbance propagates southward along the coast of South America and northwestward along the coast of Central and North America (lower panel).

SLH at low latitudes along the South American coast during the most recent El Niño is shown in Figure 13. The data have been low-pass filtered to display SLH variability at two time scales: $\geq$ 2 days (thin line) and $\geq$ 30 days (heavy line). Seasonal variability of SLH in this region is very small (see Figure 8) and has not been removed from the data in Figure 13. Prior to the onset of El Niño, regular oscillations with an amplitude of about 5 cm and a periodicity of about 45 days are present at all three stations shown in Figure 13. The source of this variability is presently under investigation, but it is probably unrelated to El Niño. The most prominent feature of Figure 13 is the rapid rise in SLH at all three stations beginning in September 1982, two months following the collapse of the trade winds in the western tropical Pacific. By January 1983, SLH had risen approximately 50 cm.

Because the seasonal variability of SLH is so small in this region (less than 5 cm), a signal as large as that observed in 1982–1983 is particularly easy to identify. It is thus not surprising that the effects of El Niño have long been apparent in the eastern tropical Pacific. Until the last 5 years or so, it was not recognized that El Niño effects can be identified at higher latitudes as well. This is because the interannual variability associated with El Niño at mid- to high latitudes tends to be masked by seasonal and other background variability with comparable or larger amplitude.

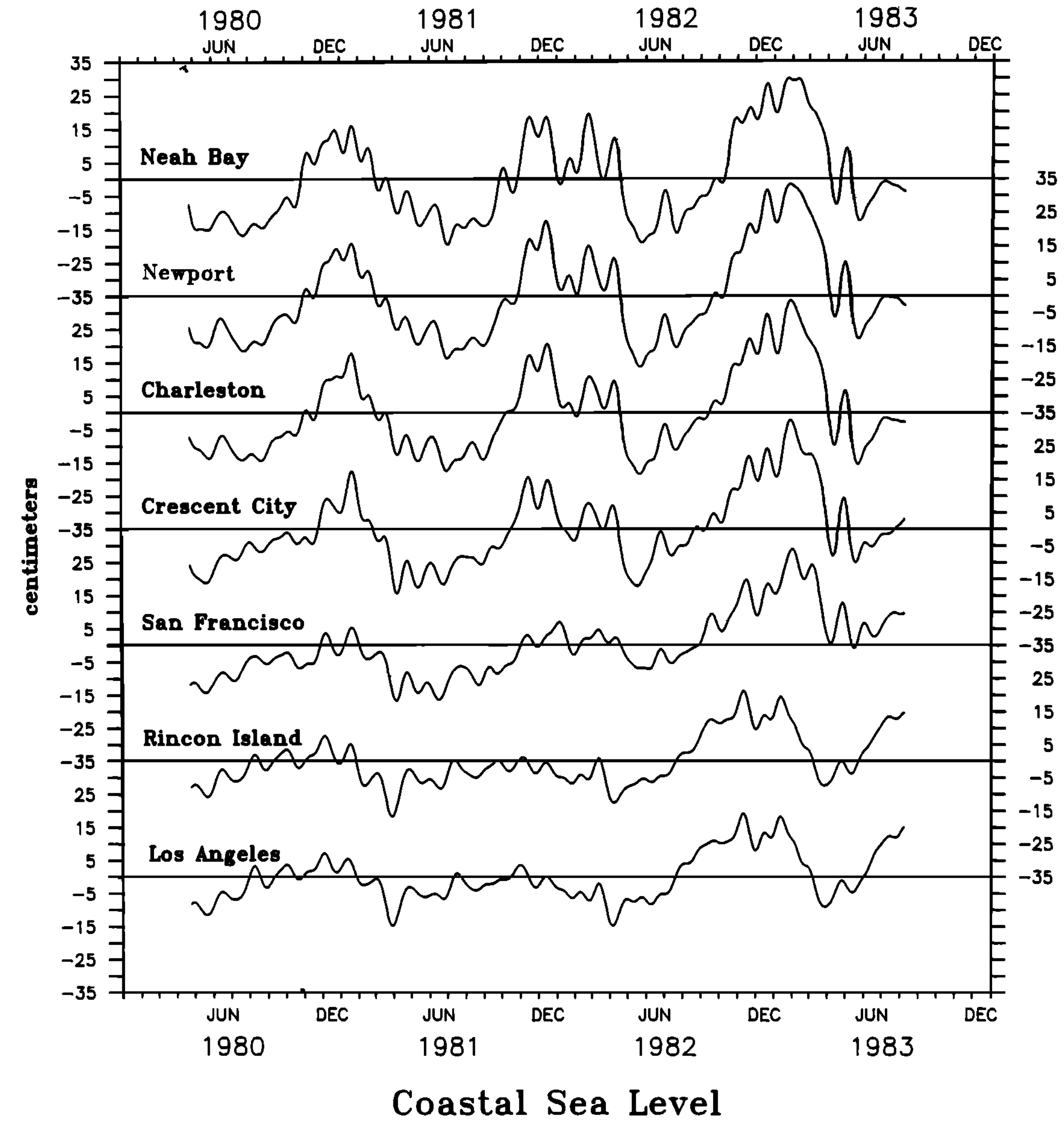

Fig. 14. Low-pass-filtered (half power point at 30 days) sea level (in centimeters) during 1980–1983 at seven stations along the west coast of the United States. The data have been corrected for tides and the inverted barometer effect.

As discussed previously (Figure 12), the El Niño signal in SLH in the eastern tropical Pacific should lead to similar SLH anomalies along the west coast of the United States, after an appropriate time lag to allow for poleward propagation. SLH variability at seven stations from Los Angeles to Neah Bay is shown in Figure 14 for mid-1980 to mid-1983. These data have been corrected for inverted barometer affects, but the seasonal cycles have not been removed. The most pronounced feature at all stations is a strong seasonal variability with highest SLH generally occurring in winter and lowest SLH in summer. The amplitude of this seasonal variability increases poleward. As discussed previously (section 7), this seasonal variability is due to the effects of nearshore geostrophic currents. Superimposed on this strong seasonal variability are numerous events with time scales of 1–2 months which may represent the effects of low-frequency atmospheric forcing discussed in section 8.

For the discussion here, the most important feature in Figure 14 is the strong interannual variability apparent at all seven stations. Winter SLH is higher during 1982–1983 than in either of the preceding winters (see also Figure 1*d*). In fact, SLH at most of these stations was the highest ever recorded during winter 1982–1983. The timing of this anomalously high SLH is suggestive of a relation to the El Niño of 1982. Indeed, Figure 14 indicates a progression from south to north; the highest SLH appeared around November 1982 at Los Angeles and around January 1983 at Neah Bay. Thus, although not as apparent as along the tropical South American coast where the background SLH variability is smaller, the El Niño signal can be detected in SLH records at higher latitudes as well. The El Niño signal becomes more apparent after removing the seasonal cycle. For example, the El Niño events of 1957–1958, 1965, 1969–1970, and 1972–1973 are evident in SLH anomalies at all 19 stations in Figure 9.

The relation between El Niño occurrences in the tropical Pacific and SLH along the west coast of North America has been examined statistically by *Enfield and Allen* [1980] and *Chelton and Davis* [1982]. Based on the El Niño events which

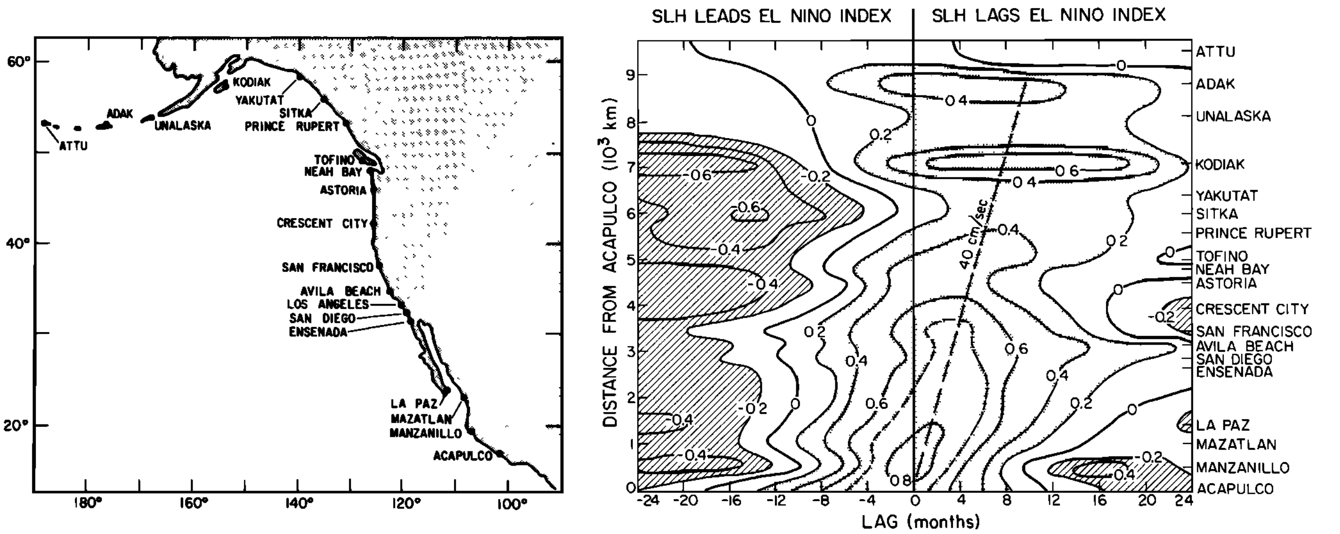

Fig. 15. Contour plot of the correlation between an index of El Niño in month t and sea level in month (t + LAG) at 20 stations along the west coast of North America. Dashed line represents 40 cm/s poleward propagation [from *Chelton and Davis*, 1982].

occurred between 1945 and 1975, the time-lagged correlation between SST in the eastern tropical Pacific (an index of El Niño) and anomalous SLH at 20 stations along the west coast of North America is contoured in Figure 15. The contoured correlations indicate a definitive asymmetry in the correlation with equatorial SST leading SLH to the north. The amount by which SST leads SLH increases in a fairly systematic manner with increasing distance along the coastline. The El Niño signal in eastern tropical Pacific SST occurs nearly simultaneously with Acapulco SLH but appears to lead San Francisco SLH by about 4 months. For reference, the dashed line in Figure 15 corresponds to a poleward phase speed of 40 cm s^{-1} ($\sim$35 km d^{-1}). *Chelton et al.* [1982] have shown that this El Niño signal in SLH is associated with changes in the nearshore geostrophic currents, consistent with the picture shown in Figure 4.

In summary, it is easy to identify the El Niño signal in SLH along the west coast of North America by its large coherence scale and correlation with tropical variability. Typical amplitudes of El Niño signals in the tide gauge records are 10–50 cm. These signals can be easily quantified by empirical orthogonal function analysis. The first mode very accurately represents the El Niño signal [see *Chelton and Davis*, 1982]. It is thus a simple matter to remove this signal from all of the tide gauge records using an empirical orthogonal function decomposition. The El Niño signal accounts for 50–70% of the variability in anomalous SLH at stations south of Los Angeles and 10–50% of the variability at stations to the north.

10. Secular Variability

At most SLH stations there is long-term secular variability superimposed on the oceanic signals discussed in the preceding sections. Such long-term variability manifests itself as quasi-linear trends in the time series. Because the secular trends are small, record lengths of 10 years or more are necessary for the signal to stand out above the background variability. The rates of secular rise or fall (determined by least squares regression on a linear trend) at the 20 stations shown in Figure 15 are plotted in Figure 16. The trends are not the same at all locations and, in fact, differ in sign from one location to another. This is suggestive that these long-term trends are not due entirely to oceanic effects.

Secular SLH variability along the Pacific coast of the United States has been previously studied by *Hicks and Shofnos* [1965] and *Roden* [1966]. Since SLH is recorded relative to a fixed bench mark, trends in SLH indicate either actual changes in the water level or changes in the level of the bench mark relative to a geoid. An uplift of the land mass, for example, would cause the bench mark to rise and result in an apparent drop in SLH. At most locations, SLH has been rising over the last half century. It has been argued that much of this increase in SLH is due to the eustatic rise in sea level from an increase in the water volume of the oceans from melting glaciers and ice sheets [*Gutenberg*, 1941; *Munk and Revelle*, 1952; *Meier*, 1983, 1984]. In an early study of SLH records at 69 locations distributed throughout the world, *Gutenberg* [1941] estimated that SLH rose at an average rate of 0.1 cm/yr over the early part of this century. Analyzing an additional 30 years of data at 27 stations along the east and west coasts of the United States, *Hicks* [1978] estimated a eustatic SLH rise of about 0.15 cm/yr. Most recently, *Barnett* [1984] analyzed SLH at 155 stations distributed throughout the world and concluded that (1) there was little or no secular

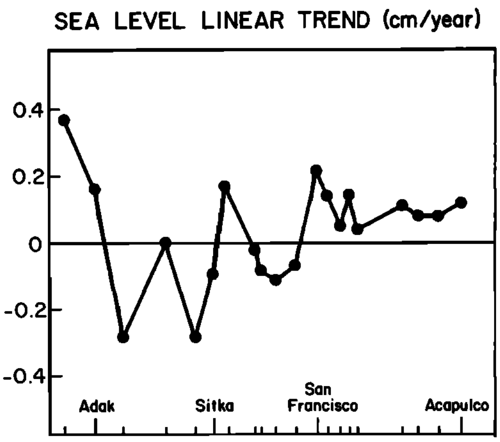

Fig. 16. Rate of linear trend in sea level (in centimeters per year) as determined by least squares regression at each of the 20 tide gauge stations shown in Figure 15. Tic marks on lower axis correspond to approximate relative alongshore spatial location of the 20 stations (see right-hand axis in Figure 15) [after *Chelton and Davis*, 1982].

TABLE 2. Summary of Ocean Signals in Tide Gauge Records and Comments on Ease of Removal From the Data

Signal	Amplitude, cm	Comments
Tides	100–200	easily removed by harmonic analysis or low pass filtering
Inverse barometer effect	1–10	mostly removed by adding 1.01 cm/mbar of atmospheric pressure (the exact validity of this correction remains questionable)
Geostrophic currents	1–100	result from many causes; some are easily removed (e.g., seasonal variability or El Niño) and others are difficult to remove (e.g., coastal upwelling or coastal trapped waves)
Coastal upwelling	10–20	difficult to remove since response to wind varies with stratification in the water column; significantly reduced by low-pass filtering
Coastal trapped waves	10–20	difficult to remove since amplitude and phase speed depend on quantities which cannot be adequately measured along propagation path; significantly reduced by low-pass filtering
Seasonal variability	1–40	easily removed from monthly average data by long-term average method or harmonic analysis
Low-frequency atmospheric forcing	1–4	easily removed by multivariate regression analysis
El Niño effect	10–50	easily removed by empirical orthogonal function analysis
Secular variability	1–10	easily removed by regression on linear trend but difficult to separate oceanic contributions from that due to crustal motion

trend prior to the early 1900s, (2) the slope of the SLH trend over the full period 1891–1980 is 0.14 cm/yr, and (3) the eustatic rise has been 0.23 cm/yr since 1930. There is strong concern that the apparent increase in rate of SLH rise in recent years may be a consequence of global warming from increased CO_2 in the atmosphere [*Madden and Ramanathan*, 1980; *Gornitz et al.*, 1982].

In contrast to the rising SLH observed over most of the world ocean, SLH has been falling along the southeastern coast of Alaska, in Scandinavia, and in the Hudson Bay region [*Gutenberg*, 1941]. This is generally thought to be due to an emergence of the land in these regions as a result of isostatic rebound of the earth's crust from the most recent glaciation rather than a true eustatic sea level change. The land emergence in southeastern Alaska is believed to be centered near Glacier Bay, located between Yakutat and Sitka, and *Hicks and Shofnos* [1965] have estimated a 0.4 cm/yr rate of uplift from SLH records. This amounts to about twice the rate of uplift inferred from SLH records in the Hudson Bay region [*Gutenberg*, 1941].

Aside from the eustatic rise in SLH, it is often assumed that secular variability in tide gauge records is of nonoceanographic origin. However, *White et al.* [1979] have shown from the vertical distribution of temperature and salinity that computed steric sea level over the entire western North Pacific has decreased 2–4 cm over the period from 1954 to 1972 due to a reduction of heat content of the upper ocean. Unfortunately, continuous records of upper ocean hydrographic data are generally not available over most of the world ocean for evaluation of the oceanographic contribution to secular variability. SST can be used as a crude measure of upper ocean heat content. *Chelton and Davis* [1982] noted a 4°C decrease in SST in the northeastern Pacific from 1958 to 1974. So it appears that variations in upper ocean heat content such as those observed by *White et al.* [1979] may occur in other areas as well. It is noteworthy that there is no evidence of secular variability in SST at lower latitudes in the eastern Pacific.

This presents some interesting suggestions about the cause of observed SLH trends at the Alaskan tide gauge stations. Without subsurface temperature measurements to compute the integrated effect of the observed decrease in upper ocean temperature, it is not possible to evaluate the relative importance of thermal effects versus isostatic rebound in causing the observed drop in SLH in the northeastern Pacific. However, if the observed 4°C decrease in water temperature at the surface extended to a mixed layer depth of 65 m (not unreasonable), the resulting drop in SLH would be one half that measured at Yakutat. A 4°C temperature drop in the upper 130 m would account for all of the measured SLH drop at Yakutat. Thus, at least from 1958, a significant portion of the secular drop in tide-gauge-measured SLH may be due to a true sea level change rather than purely isostatic rebound.

It is apparent, then, that a variety of processes may be responsible for observed secular variations in SLH. There is considerable controversy over which causes are the most important. It must be stressed that the statistical reliability of any speculations about the cause of trends is necessarily low since they effectively represent less than one complete realization of the process. The implications will not be pursued further here except to point out that estimates of the viscosity of the earth's upper mantle computed from SLH trends in southeastern Alaska must be considered to be a lower bound on the true value [e.g., *Crittenden*, 1967; *Clark*, 1977]. It is clearly difficult (if not impossible) to separate oceanographic and non-oceanographic contributions to secular SLH variability.

11. SUMMARY

We have summarized the major oceanic signals in tide gauge records. Since the primary readers of this paper will be geophysicists interested in using tide gauge records to infer vertical crustal motion, we have taken the approach that ocean signals are unwanted "noise" in the data. Accordingly, we have attempted to describe methods of removing the oceanic signals in order to isolate variability due to crustal motion. For some of the oceanic signals discussed here, removal is a relatively simple task. For others, it is very difficult. The signals discussed in this paper, their approximate amplitudes and brief comments on removal are summarized in Table 2.

In short, the following gives a reasonable plan which should be followed prior to analysis of crustal motion from tide gauge records:

1. Remove all tidal signals from the raw (usually hourly) tide gauge measurements by harmonic analysis or low-pass filtering.

2. Remove the inverted barometer effects of atmospheric pressure by adding 1.01 cm for every millibar of pressure increase.

3. Low-pass filter the data to remove high-frequency SLH variability. This filtering sacrifices temporal resolution in the data but eliminates the 2- to 10-day SLH signals from coastal upwelling and coastal-trapped waves. Note that monthly averages are not a very good method of low-pass filtering.

4. Compute and remove the seasonal cycle of SLH by harmonic analysis or long-term averages for each month of the year.

5. Remove the effects of large-scale and local low-frequency wind forcing by multivariate regression analysis.

6. Compute empirical orthogonal functions (principal components) of residual monthly anomaly SLH over a large number of stations. Remove the contribution from the most energetic mode to eliminate large-scale coherent variability such as that associated with El Niño effects.

The most difficult signal to deal with is the secular variability discussed in section 10. Part of this signal may represent glacial rebound or emergence or subsidence of the earth's crust. However, there are at least two oceanic processes which have been suggested to explain secular trends in SLH records. These are a eustatic rise in SLH from melting glaciers and ice sheets and changes in SLH due to long-term changes in the thermal structure of the upper ocean. Large-scale secular changes in salinity could generate similar signals in SLH records. We offer no suggestion for how to handle this secular variability. We only caution that assuming that all of the non-eustatic secular variability is due to crustal motion may be very misleading.

Acknowledgments. We would like to thank W. Sturges and P. Vanicek for thoughtful comments on the manuscript. We also thank Pam Wegner for typing the manuscript. This work was supported by the National Science Foundation under grants OCE-8315421 and OCE-837390 and by the National Atmospheric and Oceanic Administration under grant NA84RAD05043.

REFERENCES

Adams, J. K., and V. T. Buchwald, The generation of continental shelf waves, *J. Fluid Mech.*, *35*, 815–826, 1969.

Barnett, T. P., The estimation of "global" sea level change: A problem of uniqueness, *J. Geophys. Res.*, *89*, 7980–7988, 1984.

Blumen, W., Geostrophic adjustment, *Rev. Geophys.*, *10*, 485–528, 1972.

Brooks, D. A., and C. N. K. Mooers, Wind-forced continental shelf waves in the Florida Current, *J. Geophys. Res.*, *82*, 2569–2576, 1977.

Brown, W., W. Munk, F. Snodgrass, H. Mofield, and B. Zetler, MODE bottom experiment, *J. Phys. Oceanogr.*, *5*, 75–85, 1975.

Busalacchi, A. J., and J. J. O'Brien, Interannual variability of the equatorial Pacific in the 1980's, *J. Geophys. Res.*, *88*, 7551–7562, 1981.

Cane, M. A., Oceanographic events during El Niño, *Science*, *222*, 1189–1194, 1983.

Chelton, D. B, and R. E. Davis, Monthly mean sea-level variability along the west coast of North America, *J. Phys. Oceanogr.*, *12*, 757–784, 1982.

Chelton, D. B., P. A. Bernal, and J. A. McGowan, Large-scale interannual physical and biological interaction in the California Current, *J. Mar. Res.*, *40*, 1095–1125, 1982.

Cheney, R. E., J. G. Marsh, and B. D. Beckley, Global mesoscale variability from colinear tracks of Seasat altimeter data, *J. Geophys. Res.*, *88*, 4343–4354, 1983.

Christensen, N., R. de la Paz, and G. Gutierrez, A study of subinertial waves off the west coast of Mexico, *Deep Sea Res.*, *30*, 835–850, 1983.

Clark, J. A, An inverse problem in glacial geology: The reconstruction of glacier thinning in Glacier Bay, Alaska between A.D. 1910 and 1960 from relative sea level data, *J. Glaciol.*, *18*, 481–503, 1977.

Clarke, A. J., Observational and numerical evidence for wind-forced coastal trapped long waves, *J. Phys. Oceanogr.*, *7*, 231–247, 1977.

Crittenden, M. D., Viscosity and finite strength of the mantle as determined from water and ice loads, *Geophys. J. R. Astron. Soc.*, *14*, 261–279, 1967.

Davis, R. E., Predictability of sea surface temperature and sea level pressure anomalies over the North Pacific Ocean, *J. Phys. Oceanogr.*, *6*, 249–266, 1976.

de Szoeke, R. A., and J. G. Richman, The role of wind-generated mixing in coastal upwelling, *J. Phys. Oceanogr.*, *11*, 1234–1547, 1981.

de Szoeke, R. A., and J. G. Richman, On wind-driven mixed layers with strong horizontal gradients—A theory with application to coastal upwelling, *J. Phys. Oceanogr.*, *14*, 364–377, 1984.

Doodson, A. T., The harmonic development of the tide-generating potential, *Proc. R. Soc. London, Ser. A*, *100*, 305–329, 1922.

Ekman, V. W., On the influence of the earth's rotation on ocean currents, *Ark. Mat., Astron. Fys.*, *2*, 1–53, 1905.

Enfield, D. B., El Niño: Pacific eastern boundary response to interannual forcing, in *Resource Management and Environmental Uncertainty: Lessons from Coastal Upwelling Fisheries*, edited by M. H. Glantz and J. D. Thompson, pp. 213–254, Wiley-Interscience, New York, 1981.

Enfield, D. B., and J. S. Allen, On the structure and dynamics of monthly mean sea level anomalies along the Pacific coast of North and South America, *J. Phys. Oceanogr.*, *10*, 557–578, 1980.

Enfield, D. B., and J. S. Allen, The generation and propagation of sea level variability along the Pacific coast of Mexico, *J. Phys. Oceanogr.*, *13*, 1012–1033, 1983.

Fu, L.-L., and D. B. Chelton, Temporal variability of the Antarctic Circumpolar Current observed from satellite altimetry, *Science*, *226*, 343–346, 1984.

Fu, L.-L., and D. B. Chelton, Observing large-scale temporal variability of ocean currents by satellite altimetry; with application to the Antarctic Circumpolar Current, *J. Geophys. Res.*, *90*, 4721–4739, 1985.

Gill, A. E., and E. H. Schumann, The generation of long shelf waves by the wind, *J. Phys. Oceanogr.*, *4*, 83–90, 1974.

Gornitz, V., L. Lebedefl, and J. Hansen, Global sea level trend in the past century, *Science*, *215*, 1611–1614, 1982.

Gutenberg, B., Changes in sea level, postglacial uplift, and mobility of the earth's interior, *Geol. Soc. Am. Bull.*, *52*, 721–772, 1941.

Halliwell, G. R., and J. S. Allen, Large-scale sea level response to atmospheric forcing along the west coast of North America, summer 1973, *J. Phys. Oceanogr.*, *14*, 864–886, 1984.

Hicks, S., An average geopotential sea level series for the United States, *J. Geophys. Res.*, *70*, 3315–3320, 1978.

Hicks, S., and W. Shofnos, The determination of land emergence from sea level observations in southeast Alaska, *J. Geophys. Res.*, *70*, 3315–3320, 1965.

Hurlburt, H. E., J. D. Kindle, and J. J. O'Brien, A numerical simulation of the onset of El Niño, *J. Phys. Oceanogr.*, *6*, 621–631, 1976.

Madden, R. A., and V. Ramanathan, Detecting climatic change due to increasing carbon dioxide, *Science*, *209*, 763–768, 1980.

Marsh, J. G., and T. V. Martin, The SEASAT altimeter mean sea surface model, *J. Geophys. Res.*, *87*, 3269–3280, 1982.

McCreary, J. P., Eastern tropical ocean response to changing wind systems: With application to El Niño, *J. Phys. Oceanogr.*, *6*, 632–645, 1976.

Meade, R. H., and K. O. Emery, Sea level as affected by river runoff, eastern United Seates, *Science*, *173*, 425–427, 1971.

Meier, M. F., Snow and ice in a changing hydrological world, *J. Hydrol. Sci.*, *28*, 3–22, 1983.

Meier, M. F., Contribution of small glaciers to global sea level, *Science*, *226*, 1418–1421, 1984.

Montgomery, R. B., Fluctuations in monthly sea level on eastern U.S. coast as related to dynamics of western North Atlantic Ocean, *J. Mar. Res.*, *1*, 165–185, 1938.

Munk, W. H., and D. E. Cartwright, Tidal spectroscopy and prediction, *Philos. Trans. R. Soc. London*, *259*, 533–581, 1966.

Munk, W., and R. Revelle, Sea level and the rotation of the earth, *Am. J. Sci.*, *250*, 829–833, 1952.

Mysak, L. A., and B. V. Hamon, Low frequency sea level behavior and continental shelf waves off North Carolina, *J. Geophys. Res.*, *74*, 1397–1405, 1969.

O'Brien, J. J., A. Busalacchi, and J. Kindle, Ocean models of El Niño, in *Resource Management and Environmental Uncertainty: Lessons from Coastal Upwelling Fisheries*, edited by M. H. Glantz and J. D. Thompson, pp. 159–212, Wiley-Interscience, New York, 1981.

Pattullo, J., W. Munk, R. Revelle, and E. Strong, The seasonal oscillation in sea level, *J. Mar. Res.*, *14*, 88–155, 1955.

Philander, S. G. H., El Niño Southern Oscillation phenomena, *Nature*, *302*, 295–301, 1983.

Pond, S., and G. L. Pickard, *Introductory Dynamic Oceanography*, 241 pp., Pergamon, New York, 1978.

Rasmusson, E. M., and T. M. Carpenter, Variations in tropical sea surface temperature and surface wind fields associated with the southern oscillation/El Niño, *Mon. Weather Rev.*, *110*, 354–384, 1982.

Reid, J. L., On the geostrophic flow at the sea surface of the Pacific Ocean with respect to the 1000 decibar surface, *Tellus*, *8*, 489–502, 1961.

Reid, J. L., and R. S. Arthur, Interpretation of maps of geopotential anomaly for the deep Pacific Ocean, *J. Mar. Res.*, *33*, 37–52, 1975.

Reid, J. L., and A. W. Mantyla, The effect of the geostrophic flow upon coastal sea level variations in the northern Pacific Ocean, *J. Geophys. Res.*, *81*, 3100–3110, 1976.

Robinson, A. R., Continental shelf waves and the response of sea level to weather systems, *J. Geophys. Res.*, *69*, 367–368, 1964.

Roden, G. I., On atmospheric pressure oscillations along the Pacific coast of North America, 1873–1963, *J. Atmos. Sci.*, *22*, 280–295, 1965.

Roden, G. I., Low frequency sea level oscillations along the Pacific coast of North America, *J. Geophys. Res.*, *71*, 4755–4775, 1966.

Royer, T. C., On the effect of precipitation and runoff on coastal circulation in the Gulf of Alaska, *J. Phys. Oceanogr.*, *9*, 555–563, 1979.

Royer, T. C., Baroclinic transport in the Gulf of Alaska, II, A fresh water driven coastal current, *J. Mar. Res.*, *39*, 251–266, 1981.

Saur, J. F. T., The variability of monthly mean sea level at six stations in the eastern North Pacific Ocean, *J. Geophys. Res.*, *67*, 2781–2790, 1962.

Schopf, P. S., and D. E. Harrison, On equatorial waves and El Niño, I, Influence of initial states on wave-induced currents and warming, *J. Phys. Oceanogr.*, *13*, 936–948, 1983.

Smith, R. L., Poleward propagating perturbations in currents and sea levels along the Peru coast, *J. Geophys. Res.*, *83*, 6083–6092, 1978.

Stommel, H., P. Niiler, and D. Anati, Dynamic topography and the recirculation of the North Atlantic, *J. Mar. Res.*, *36*, 449–468, 1978.

Sturges, W., Sea level slope along continental boundaries, *J. Geophys. Res.*, *79*, 825–830, 1974.

Tapley, B. D., G. H. Born, and M. E. Parke, The Seasat altimeter data and its accuracy assessment, *J. Geophys. Res.*, *87*, 3179–3188, 1982.

Vanicek, P., To the problem of noise reduction in sea-level records used in vertical crustal movement detection, *Phys. Earth Planet. Inter.*, *17*, 265–280, 1978.

Wahr, J., and M. Wyss, Interpretation of postseismic deformation with a viscoelastic relaxation model, *J. Geophys. Res.*, *85*, 6471–6477, 1980.

Wang, D. P., and C. N. K. Mooers, Long coastal-trapped waves off the west coast of the United States, summer 1973, *J. Phys. Oceanogr.*, *7*, 856–864, 1977.

White, W. B., and K. Hasanuma, Interannual variability in the baroclinic gyre structure of the western North Pacific from 1954–1974, *J. Mar. Res.*, *38*, 651–672, 1980.

White, W., K. Hasunuma, and G. Meyers, Large scale secular trend in steric sea level over the western North Pacific from 1954–1974, *J. Geod. Soc. Jpn.*, *25*, 49–55, 1979.

Wunsch, C., Bermuda sea level in relation to tides, weather and baroclinic fluctuations, *Rev. Geophys.*, *10*, 1–49, 1972.

Wyrtki, K., The dynamic topography of the Pacific Ocean and its fluctuations, *Rep. HIG-74-5*, 19 pp., 37 figs., Hawaii Inst. of Geophys., Honolulu, 1974.

Wyrtki, K., Sea level during the 1972 El Niño, *J. Phys. Oceanogr.*, *7*, 779–787, 1977.

Wyrtki, K., The response of sea surface topography to the 1976 El Niño, *J. Phys. Oceanogr.*, *9*, 1223–1231, 1979.

Wyrtki, K., Sea level fluctuations in the Pacific during the 1982–1983 El Niño, *Geophys. Res. Lett.*, *12*, 125–128, 1985.

D. B. Chelton and D. B. Enfield, College of Oceanography, Oregon State University, Corvallis, OR 97331.

(Received April 15, 1985;
revised December 10, 1985;
accepted December 17, 1985.)